Received: 18 November 2021 | Revised: 9 July 2022 | Accepted: 12 July 2022

DOI: 10.1002/nme.7077

RESEARCH ARTICLE

WILEY

A finite element level set method based on adaptive octree meshes for thermal free-surface flows

Songzhe Xu[1] | Qiming Zhu[2] | Milinda Fernando[3] | Hari Sundar[3]

[1]State Key Laboratory of Advanced Special Steels School of Materials Science and Engineering, Shanghai University, Shanghai, China

[2]Department of Civil and Environmental Engineering, University of Illinois at Urbana-Champaign, Urbana, Illinois, USA

[3]School of Computing, University of Utah, Salt Lake City, Utah, USA

Correspondence
Songzhe Xu, State Key Laboratory of Advanced Special Steels School of Materials Science and Engineering, Shanghai University, Shanghai, China
Email: songzhex@shu.edu.cn

Funding information
Extreme Science and Engineering Discovery Environment (XSEDE), Grant/Award Number: TG-MSS200020

Abstract

We develop a parallel finite element computational framework based on the level set method and adaptive octree meshes for free-surface flows. The discretized governing formulations are stabilized using a residual-based variational multiscale method. We redistance the level set field and restore mass conservation after each time step. The octree mesh is adaptively refined according to the interface location, and the load is rebalanced across processes. The adaptive octree-based level set method is verified and validated using a canonical problem of dam break without obstacle, and a mesh convergence study is carried out in this problem. The surface tension is further considered via a continuum surface force model in the method and validated using a problem of single bubble rising in ambient liquid. A parallel scaling analysis of this method is also performed for the bubble rising problem. The energy equation and Marangoni effect are finally considered in the method and validated using a problem of thermocapillary droplet migration with and without gravity. This work illustrates the ability of the framework to accurately model and predict free-surface flows under various scenarios.

KEYWORDS

adaptive octree-based mesh, free-surface flows, level set method, residual-based variational multiscale method

1 | INTRODUCTION

Numerical simulations are important tools to study free-surface flow systems in various environmental problems and industrial applications, such as gas dissolution and transport, water supply, off-shore wind turbines, flood propagation, etc. One challenge in free-surface flow computation is the treatment of the gas-liquid interface. Two types of methods, that is, interface-tracking and interface-capturing, are mostly used in free-surface flow computations.[1,2] Interface-tracking methods utilize an explicit deformable mesh to represent the free-surface shape, and the mesh moves with free-surface deformation. Arbitrary Lagrangian–Eulerian (ALE) methods,[3] boundary-integral methods[4] and front-tracking methods[5] belong to this category. Interface-tracking method can achieve higher accuracy for resolving the interface compared with interface-capturing method. Interface-tracking method has shown its capabilities in solving additive manufacturing[6,7] and off-shore engineering problems. However, it is necessary to use robust mesh motion and re-meshing methods to manage singular topological changes of the free surface. On the other hand, interface-capturing method leverages one extra variable to implicitly represent the free surface. Front-capturing method,[8] phase field,[9,10] volume of fluid

(VOF),[11] diffuse-interface method[12,13] and level set method[14,15] belong to this type. Interface-capturing method has advantages for problems with large interface deformation, because it can automatically deal with topological changes. Interface-capturing method has been applied to challenging engineering problems in marine engineering,[16,17] jet atomization[18] and bubble dynamics.[19-21] In this paper, we utilize the level set interface-capturing method based on a large-scale finite element framework for modeling free-surface flows.

Level set method requires a higher mesh resolution near the gas-liquid interface due to the smeared treatment of the interface. The free surface position changes over time, and therefore it is challenging to use a pre-refined mesh in free surface simulation. Adaptively refining mesh will not only reduce the computational cost, but also keep the high accuracy near the gas-liquid interface. In this work, to achieve adaptive mesh refinement, an octree-based spatial discretization is employed to leverage its data structure for efficiently refining and coarsening elements according to interface location, and re-distributing elements over processes for load balancing in high performance computing. While the concept of octree-based adaptive space discretization is well studied, integrating level set method on octree-based meshes on distributed systems for simulating thermal free-surface flows is novel. Octree-based meshing has been successfully applied to finite element computations for many engineering problems.[22-27] In this work, we employ the optimized parallel octree-based meshing library, DENDRO, which has been deployed for simulating binary black hole inspiral, four-dimensional space-time tree-based adaptivity, tracking particles in channels using an immersogeometric method, simulating two-phase flows using energy stable and conservative schemes, and industrial scale large eddy simulations (LES).[28-32] Detailed features of DENDRO can be found in References 33-37. The original adaptive mesh refinement and subsequent intergrid transfer algorithms in DENDRO is adjusted for tracking the interface in simulating thermal free-surface flows.

The proposed octree-based level set framework further incorporates a residual-based variational multiscale formulation (RBVMS)[38] to solve the coupled Navier–Stokes, level set and energy equations. The RBVMS approach splits the space into coarse and fine scales using variational projections and focuses on modeling the fine-scale equations. Unlike traditional scale-split approaches, such as LES, no eddy viscosity models are needed in RBVMS method. Thus it is able to perform accurate flow condition agnostic simulations. The RBVMS method has been widely extended to various engineering applications involving computational fluid dynamics,[39-43] and it has also been successively applied to level set method to model complex multiphase flows.[44-49]

This paper is outlined as follows. Section 2 introduces the governing equations of incompressible free-surface flows. Section 3 describes the spatial semi-discrete formulations and other necessary numerical treatments. Section 4 briefs the implementation of adaptively refining the octree meshes based on interface location and subsequent intergrid transfer. In Section 5, we verify and validate the proposed framework using multiple examples including dam break without obstacle, single bubble rising in ambient liquid and thermocapillary droplet migration. Finally, we draw conclusions and motivate future research directions in Section 6.

2 | STRONG FORMULATIONS OF THE CONTINUOUS PROBLEM

We consider a gas–liquid system and describe the governing equations for this multiphase system of fluid mechanics in the following subsections.

2.1 | Phase separation

We use a level set method to distinguish gas phase and liquid phase. Let Ω denote the spatial domain occupied by a gas–liquid system with its boundary denoted as Γ. The level set equation can be written as

$$\frac{\partial \phi}{\partial t} + \boldsymbol{u} \cdot \nabla \phi = 0. \tag{1}$$

$\phi = \phi(\boldsymbol{x}, t)$ is the level set field, where $\boldsymbol{x}$ is an arbitrary point inside Ω, and $\boldsymbol{u}$ is velocity. The gas–liquid interface Γ_{g-l} can be implicitly expressed as

$$\Gamma_{g-l} = \{x \in \Omega \mid \phi(\boldsymbol{x}, t) = 0\}. \tag{2}$$

We prescribe that ϕ takes negative value in the gas phase, while it takes positive value in the liquid phase. A Heaviside function $H(\phi)$ can be then defined as

10970207, 2022, 22, Downloaded from https://onlinelibrary.wiley.com/doi/10.1002/nme.7077 by Harbin Insitute Of Technology, Wiley Online Library on [26/08/2023]. See the Terms and Conditions (https://onlinelibrary.wiley.com/terms-and-conditions) on Wiley Online Library for rules of use; OA articles are governed by the applicable Creative Commons License

$$H(\phi) = \begin{cases} 1 & \phi > 0 \\ 0.5 & \phi = 0 \\ 0 & \phi < 0\,. \end{cases} \tag{3}$$

A given material property χ at an arbitrary point inside the domain can be then computed by the auxiliary of above defined Heaviside function and can be written as

$$\chi\,(\phi) = \chi_g\,(1 - H(\phi)) + \chi_l H(\phi), \tag{4}$$

where χ_g and χ_l are the given material properties in the gas and liquid phases, respectively.

2.2 | Navier–Stokes equations

The incompressible flow motion governed by the Navier–Stokes equations may be written as

$$\rho\,(\phi)\left(\frac{\partial \boldsymbol{u}}{\partial t} + \boldsymbol{u}\cdot\nabla\boldsymbol{u}\right) = \nabla\cdot\boldsymbol{\sigma} + \boldsymbol{f} \tag{5}$$

$$\nabla\cdot\boldsymbol{u} = 0, \tag{6}$$

where ρ is the density, which is a function of ϕ. $\boldsymbol{f}$ is the forcing term, and $\boldsymbol{\sigma}$ is the Cauchy stress, defined as

$$\boldsymbol{\sigma}(\boldsymbol{u}, p) = -p\boldsymbol{I} + 2\mu\boldsymbol{\varepsilon} \tag{7}$$

$$\boldsymbol{\varepsilon}(\boldsymbol{u}) = \frac{1}{2}\left(\nabla\boldsymbol{u} + \nabla\boldsymbol{u}^{\mathrm{T}}\right), \tag{8}$$

where p is the pressure, μ is the dynamic viscosity, $\boldsymbol{\varepsilon}$ is the strain-rate tensor, and $\boldsymbol{I}$ is the identity matrix.

The forcing term $\boldsymbol{f}$ is the union of body force $\boldsymbol{f}_b$ and gas–liquid interfacial force $\boldsymbol{f}_{g-l}$, defined as $\boldsymbol{f} = \boldsymbol{f}_b + \boldsymbol{f}_{g-l}$. In this work, we consider $\boldsymbol{f}_b$ only includes the gravity, written as $\boldsymbol{f}_b\,(\phi) = \rho(\phi)\mathbf{g}$, where $\mathbf{g}$ is the gravity acceleration. We consider $\boldsymbol{f}_{g-l}$ includes surface tension and Marangoni stress, which may be written as

$$\boldsymbol{f}_{g-l}\,(T) = \sigma_s\kappa_s\mathbf{n}_s + \frac{d\sigma_s}{dT}\left(\nabla T - (\nabla T\cdot\mathbf{n}_s)\,\mathbf{n}_s\right), \tag{9}$$

where σ_s is the surface tension coefficient, κ_s is the mean curvature, defined as $\kappa_s = -\nabla\cdot\mathbf{n}_s$, $\frac{d\sigma_s}{dT}$ is the Marangoni coefficient, $\mathbf{n}_s$ is unit normal vector to the interface, and T is temperature. We will discuss $\boldsymbol{f}_{g-l}$ more in the Section 3.4.

2.3 | Energy equation

The energy equation can be written as

$$\rho(\phi)c_p(\phi)\left(\frac{\partial T}{\partial t} + \boldsymbol{u}\cdot\nabla T\right) = \nabla\cdot\left(\kappa\,(\phi)\,\nabla T\right), \tag{10}$$

where c_p is the specific heat and κ is the thermal conductivity.

The formulations (1)–(10) are accompanied with specific boundary conditions, defined on $\Gamma = \Gamma^{\mathrm{D}} \cup \Gamma^{\mathrm{N}}$ with Dirichlet boundary $\Gamma^{\mathrm{D}} = \Gamma^{\mathrm{D}}_{\boldsymbol{u}} \cup \Gamma^{\mathrm{D}}_{T}$ and Neumann boundary $\Gamma^{\mathrm{N}} = \Gamma^{\mathrm{N}}_{\boldsymbol{u}} \cup \Gamma^{\mathrm{N}}_{T}$:

$$\boldsymbol{u} = \boldsymbol{u}_d \quad \text{on } \Gamma^{\mathrm{D}}_{\boldsymbol{u}}\ , \tag{11}$$

$$T = T_{\mathrm{d}} \quad \text{on } \Gamma^{\mathrm{D}}_{T}\ , \tag{12}$$

$$-p\,\mathbf{n} + 2\mu\,\boldsymbol{\varepsilon}\cdot\mathbf{n} = \mathbf{h}_{\boldsymbol{u}} \quad \text{on } \Gamma^{\mathrm{N}}_{\boldsymbol{u}}\ , \tag{13}$$

$$\kappa\nabla T\cdot\mathbf{n} = \mathrm{h}_T \quad \text{on } \Gamma^{\mathrm{N}}_{T}\ , \tag{14}$$

where $\boldsymbol{u}_d$ and T_d denote the prescribed velocity and temperature at the Dirichlet boundaries $\Gamma^{\mathrm{D}}_{\boldsymbol{u}}$ and Γ^{D}_{T}, respectively, $\mathbf{h}_{\boldsymbol{u}}$ and h_T are the traction vector and heat flux at the Neumann boundaries $\Gamma^{\mathrm{N}}_{\boldsymbol{u}}$ and Γ^{N}_{T}, respectively, and $\mathbf{n}$ is the unit normal vector to the boundary.

10970207, 2022, 22, Downloaded from https://onlinelibrary.wiley.com/doi/10.1002/nme.7077 by Harbin Insitute Of Technology, Wiley Online Library on [26/08/2023]. See the Terms and Conditions (https://onlinelibrary.wiley.com/terms-and-conditions) on Wiley Online Library for rules of use; OA articles are governed by the applicable Creative Commons License

3 | DISCRETIZED WEAK FORMULATIONS

3.1 | RBVMS semi-discrete formulations

Let $\mathcal{W}^h$ and $\mathcal{V}^h$ be the finite-dimensional spaces of discrete test functions and trial solutions, which are denoted as superscript h, and represent resolved scales (coarse scale) produced by the finite element discretization. Following the development from Yan et al.,[48] the strong problem (1)–(14) can be recast in a weak form and posed over these discrete spaces to produce the following spatial semi-discrete problem using the VMS modeling approach: find $\{\boldsymbol{u}^h, p^h, \phi^h, T^h\} \in \mathcal{V}^h$, such that $\forall\{\mathbf{w}^h, q^h, \eta^h\ \psi^h\} \in \mathcal{W}^h$,

$$\boldsymbol{B}^{\text{VMS}}\left(\{\mathbf{w}^h, q^h, \eta^h, \psi^h\}, \{\boldsymbol{u}^h, p^h, \phi^h, T^h\}\right) - \boldsymbol{F}^{\text{VMS}}\left(\{\mathbf{w}^h, q^h, \eta^h, \psi^h\}, \{\boldsymbol{u}^h, p^h, \phi^h, T^h\}\right) = 0, \tag{15}$$

where the bilinear form $\boldsymbol{B}^{\text{VMS}}$ and forcing term $\boldsymbol{F}^{\text{VMS}}$ are given as

$$\begin{aligned}
&\boldsymbol{B}^{\text{VMS}}\left(\{\mathbf{w}^h, q^h, \eta^h, \psi^h\}, \{\boldsymbol{u}^h, p^h, \phi^h, T^h\}\right)\\
&= \int_\Omega \boldsymbol{w}^h \cdot \rho\left(\frac{\partial \boldsymbol{u}^h}{\partial t} + \boldsymbol{u}^h \cdot \nabla \boldsymbol{u}^h\right) d\Omega + \int_\Omega \nabla \boldsymbol{w}^h : \boldsymbol{\sigma}\left(\boldsymbol{u}^h, p^h\right)\ d\Omega\\
&\quad + \int_\Omega q^h \nabla \cdot \boldsymbol{u}^h d\Omega\\
&\quad + \int_\Omega \eta^h \left(\frac{\partial \phi^h}{\partial t} + \boldsymbol{u}^h \cdot \nabla \phi^h\right) d\Omega\\
&\quad + \int_\Omega \psi^h \rho C_p \left(\frac{\partial T^h}{\partial t} + \boldsymbol{u}^h \cdot \nabla T^h\right) d\Omega + \int_\Omega \nabla \psi^h \cdot \kappa \nabla T^h d\Omega\\
&\quad - \sum_{e=1}^{nel} \int_{\Omega_e} \left(\rho \boldsymbol{u}^h \cdot \nabla \boldsymbol{w}^h + \nabla q^h\right) \cdot \boldsymbol{u}'\ d\Omega - \sum_{e=1}^{nel} \int_{\Omega_e} \nabla \cdot \boldsymbol{w}^h p' d\Omega\\
&\quad + \sum_{e=1}^{nel} \int_{\Omega_e} \rho \boldsymbol{w}^h \cdot \left(\boldsymbol{u}' \cdot \nabla \boldsymbol{u}^h\right) d\Omega - \sum_{e=1}^{nel} \int_{\Omega_e} \rho \nabla \boldsymbol{w}^h : \left(\boldsymbol{u}' \otimes \boldsymbol{u}'\right) d\Omega\\
&\quad - \sum_{e=1}^{nel} \int_{\Omega_e} \boldsymbol{u}^h \cdot \nabla \eta^h \phi' d\Omega\\
&\quad - \sum_{e=1}^{nel} \int_{\Omega_e} \rho C_p \boldsymbol{u}^h \cdot \nabla \psi^h T' d\Omega,
\end{aligned} \tag{16}$$

and

$$\boldsymbol{F}^{\text{VMS}}\left(\{\mathbf{w}^h, q^h, \eta^h, \psi^h\}, \{\boldsymbol{u}^h, p^h, \phi^h, T^h\}\right) \tag{17}$$

$$= \int_\Omega \boldsymbol{w}^h \cdot \boldsymbol{f}\, d\Omega + \int_{\Gamma_{\boldsymbol{u}}^N} \mathbf{w}^h \cdot \boldsymbol{h}_u\ d\Gamma + \int_{\Gamma_{\boldsymbol{T}}^N} \psi^h h_T\ d\Gamma, \tag{18}$$

where the variables with superscript primes denote the unsolved scales (fine scale) that need to be modeled and added onto the coarse scale. The fine scale variables are defined proportional to coarse scale residuals as

$$\boldsymbol{u}' = -\frac{\tau_M}{\rho}\left(\rho\left(\frac{\partial u^h}{\partial t} + \boldsymbol{u}^h \cdot \nabla \boldsymbol{u}^h\right) - \nabla \cdot \boldsymbol{\sigma}(\boldsymbol{u}^h, p^h) - \boldsymbol{f}\right), \tag{19}$$

$$p' = -\tau_C \rho \nabla \cdot \boldsymbol{u}^h, \tag{20}$$

$$\phi' = -\tau_\phi \left(\frac{\partial \phi^h}{\partial t} + \boldsymbol{u}^h \cdot \nabla \phi^h\right), \tag{21}$$

$$T' = -\frac{\tau_T}{\rho C_p}\left(\rho C_p \left(\frac{\partial T^h}{\partial t} + \boldsymbol{u}^h \cdot \nabla T^h\right) - \nabla \cdot \kappa \nabla T^h - Q_s\right), \tag{22}$$

10970207, 2022, 22, Downloaded from https://onlinelibrary.wiley.com/doi/10.1002/nme.7077 by Harbin Institute Of Technology, Wiley Online Library on [26/08/2023]. See the Terms and Conditions (https://onlinelibrary.wiley.com/terms-and-conditions) on Wiley Online Library for rules of use; OA articles are governed by the applicable Creative Commons License

where τ_M, τ_C, τ_ϕ, and τ_T are stabilization parameters given as

$$\tau_M = \left(\frac{4}{\Delta t^2} + \boldsymbol{u}^h \cdot \boldsymbol{G}\boldsymbol{u}^h + C_M \left(\frac{\mu}{\rho} \right)^2 \boldsymbol{G} : \boldsymbol{G} \right)^{-\frac{1}{2}}. \tag{23}$$

$$\tau_C = \frac{1}{tr(\boldsymbol{G})\tau_M}. \tag{24}$$

$$\tau_\phi = \left(\frac{4}{\Delta t^2} + \boldsymbol{u}^h \cdot \boldsymbol{G}\boldsymbol{u}^h \right)^{-\frac{1}{2}}. \tag{25}$$

$$\tau_T = \left(\frac{4}{\Delta t^2} + \boldsymbol{u}^h \cdot \boldsymbol{G}\boldsymbol{u}^h + C_T \left(\frac{\kappa}{\rho C_p} \right)^2 \boldsymbol{G} : \boldsymbol{G} \right)^{-\frac{1}{2}}. \tag{26}$$

In above equations, Δt is the time-step size, which can be chosen following the CFL condition. C_M and C_T are positive constants which can be derived from element-wise inverse estimates. $\boldsymbol{G}$ is a mesh-dependent quantity calculated by the mapping from the isoparametric counterpart (ξ) to the physical element ($\boldsymbol{x}$)

$$G_{ij} = \sum_{k=1}^{3} \frac{\partial \xi_k}{\partial x_i} \frac{\partial \xi_k}{\partial x_j} , \tag{27}$$

and $tr\ \boldsymbol{G}$ is the trace of $\boldsymbol{G}$. Equations (15)–(27) feature the VMS formulations of level set equation, Navier–Stokes equations and energy equation of incompressible thermal multiphase flows.

3.2 | Regularization and redistancing of level set field

The sharp gas–liquid interface is regularized in the spatial discretization in order to perform finite element computation using interface-capturing methods. A regularized Heaviside function H_r in lieu of Equation (3) is defined as

$$H_r(\phi) = \begin{cases} 1 & \phi > \epsilon \\ 0.5\left(1 + \frac{\phi}{\epsilon} + \frac{1}{\pi}\sin\left(\frac{\phi\pi}{\epsilon}\right)\right) & -\epsilon \leq \phi \leq \epsilon \\ 0 & \phi < -\epsilon\ . \end{cases} \tag{28}$$

where ϵ determines the thickness of the regularized interface, which is usually chosen as the same order of the element size across interface. In order to construct a smooth, well-structured interface, the level set field is initially adjusted to have the signed-distance property. However, the signed-distance property may be unavoidably destroyed as level set field purely evolves with velocity during time stepping, resulting in a distorted interface. As a result, a redistancing of level set field is required to restore the signed-distance property to retain a well-structured interface during the computation.

We redistance the level set field after each time step to obtain a new level set field ϕ_{rd} that satisfies the signed-distance property by solving

$$\frac{\partial \phi_{rd}}{\partial t_{rd}} + \text{sgn}(\phi)(|\nabla \phi_{rd}| - 1) = 0 \quad in \quad \Omega, \tag{29}$$

where sgn $(\cdot)$ is the sign function and $|\cdot|$ denotes the Euclidean norm, with the constraint of

$$\phi_{rd} = \phi = 0 \quad \text{on} \quad \Gamma_{g-l}, \tag{30}$$

to ensure the correct position of the gas–liquid interface during time stepping. The steady state solution of Equations (29) and (30) can be evolved from an initial condition $\phi_{rd}(\boldsymbol{x}, 0) = \phi(\boldsymbol{x})$ over pseudo time t_{rd}, and possesses the signed-distance property, that is, satisfies the Eikonal equation[50] $|\nabla \phi_{rd}| = 1$ in Ω *. Providing the solution of ϕ^h after solving the level set equation, Equations (29) and (30) can be recast in a semi-discrete weak form (using VMS) and posed over the discrete

10970207, 2022, 22, Downloaded from https://onlinelibrary.wiley.com/doi/10.1002/nme.7077 by Harbin Institute Of Technology, Wiley Online Library on [26/08/2023]. See the Terms and Conditions (https://onlinelibrary.wiley.com/terms-and-conditions) on Wiley Online Library for rules of use; OA articles are governed by the applicable Creative Commons License

spaces: Find $\phi^h_{rd} \in \mathcal{V}^h$, such that $\forall \eta^h_{rd} \in \mathcal{W}^h$,

$$\begin{aligned}
&\int_{\Omega} \eta^h_{rd}\left(\frac{\partial \phi^h_{rd}}{\partial t_{rd}} + S_{rd}\left(\phi^h_{rd}\right)\left(|\nabla\phi^h_{rd}|-1\right)\right) d\Omega \\
&\quad - \sum_{e=1}^{nel}\int_{\Omega_e} S_{rd}\left(\phi^h_{rd}\right) \frac{\nabla\phi^h_{rd}}{|\nabla\phi^h_{rd}|}\cdot\nabla\eta^h_{rd}\,\phi'_{rd}\,d\Omega \\
&\quad + \sum_{e=1}^{nel}\int_{\Omega_e}\eta^h_{rd}\lambda\frac{dH_r\left(\phi^h_{rd}\right)}{d\phi^h_{rd}}\left(\phi^h_{rd}-\phi^h\right)\,d\Omega = 0\ ,
\end{aligned} \tag{31}$$

where $S_{rd}\left(\phi^h_{rd}\right) = 2H_r\left(\phi^h_{rd}\right) - 1$, λ is the penalty parameter to enforce the constraint of $\phi^h_{rd} = \phi^h$ inside the regularized interface, and ϕ'_{rd} is the fine scale ϕ_{rd} and can be written as

$$\phi'_{rd} = -\tau_{rd}\left(\frac{\partial \phi^h_{rd}}{\partial t_{rd}} + S_{rd}\left(\phi^h_{rd}\right)\left(|\nabla\phi^h_{rd}|-1\right)\right) d\Omega, \tag{32}$$

and

$$\tau_{rd} = \left(\frac{4}{\Delta t^2_{rd}} + S_{rd}\left(\phi^h_{rd}\right)\frac{\nabla\phi^h_{rd}}{|\nabla\phi^h_{rd}|}\cdot\boldsymbol{G}\left(S_{rd}\left(\phi^h_{rd}\right)\frac{\nabla\phi^h_{rd}}{|\nabla\phi^h_{rd}|}\right)\right). \tag{33}$$

$S_{rd}\left(\phi^h_{rd}\right)\frac{\nabla\phi^h_{rd}}{|\nabla\phi^h_{rd}|}$ can be interpreted as an effective convective velocity[†] . The size of the pseudo time step Δt_{rd} may be chosen from an effective CFL condition of Equation (31).

3.3 | Mass fixing

Level set method as well as redistancing may fail to observe mass conservation. In order to conserve mass, a global mass restoration method is employed via shifting the level set field by a global constant $\Delta\phi^h$ after the redistancing, which therefore does not alter the signed-distance property obtained from re-distancing. The $\Delta\phi^h$ can be solved from

$$\int_{\Omega}\frac{\partial H_r\left(\phi^h\right)}{\partial t}\,d\Omega = -\int_{\Gamma}\left(\frac{\rho_g}{\rho_l-\rho_g} + H_r\left(\phi^h\right)\right)\boldsymbol{u}^h\cdot\mathbf{n}\,d\Gamma, \tag{34}$$

which is derived from the mass conservation law. Note, since $\Delta\phi^h$ is a global constant, a scalar nonlinear equation needs to be solved. In the temporal discrete form, $(H_r)^n$ at current time step n can be evaluated by $\left(\phi^h_{rd}\right)^n + \left(\Delta\tilde{\phi}^h\right)^n$ when using an iterative nonlinear solver, where $\left(\Delta\tilde{\phi}^h\right)^n$ is the solution of $\left(\Delta\phi^h\right)^n$ from the last nonlinear iteration in this time step. The final $\left(\phi^h\right)^n$ of current time step is updated by $\left(\phi^h_{rd}\right)^n + \left(\Delta\phi^h\right)^n$ after solving $\left(\Delta\tilde{\phi}^h\right)^n$ until convergence. $\frac{\rho_g}{\rho_l-\rho_g}$ may be omitted since liquid density is much bigger than gas density.

3.4 | Gas–liquid interfacial forces

In this work, we consider the continuum surface force (CSF) model to convert the interfacial force $\boldsymbol{f}_{g-l}(T)$ from a surface force into a continuous volume force for the regularized interface, and Equation (9) is rewritten in the discrete form as

$$\boldsymbol{f}^h_{g-l}(\phi^h, T^h) = \left(\sigma_s\kappa_s\mathbf{n}_s + \frac{d\sigma_s}{dT^h}\left(\nabla T^h - \left(\nabla T^h\cdot\mathbf{n}_s\right)\mathbf{n}_s\right)\right)\delta_r, \tag{35}$$

10970207, 2022, 22, Downloaded from https://onlinelibrary.wiley.com/doi/10.1002/nme.7077 by Harbin Institute Of Technology, Wiley Online Library on [26/08/2023]. See the Terms and Conditions (https://onlinelibrary.wiley.com/terms-and-conditions) on Wiley Online Library for rules of use; OA articles are governed by the applicable Creative Commons License

where unit normal vector $\mathbf{n}_s$ is now defined as $\mathbf{n}_s = -\frac{\nabla \phi^h}{|\nabla \phi^h|}$ at arbitrary point inside the regularized interface, and mean curvature κ_s is defined as $\kappa_s = \frac{|\nabla \phi^h|^2 tr(\boldsymbol{\Psi}(\phi^h)) - (\nabla \phi^h)^T \boldsymbol{\Psi}(\phi^h) \nabla \phi^h}{|\nabla \phi^h|^3}$. $\boldsymbol{\Psi}$ is the Hessian matrix with second derivatives, which can be evaluated by an L_2 projection when using linear basis function. δ_r is a density-scaled Dirac delta function for the regularized interface, defined as $\delta_r = \frac{2\rho(\phi^h)}{\rho_g + \rho_l} \frac{dH_r}{d\phi^h}$.

3.5 | Temporal discretization and solving strategies

We employ a fully implicit backward Euler scheme based on finite difference for the discretization of the governing equations (as well as the pseudo time-dependent Eikonal equation) in time. We employ the Newton–Raphson method to solve the nonlinear governing equations. For the thermal multiphase system, a block-iterative strategy[40] is employed to form three individual systems, one for the Navier–Stokes equations, one for the level set equation, and one for the energy equation, and solve them self-consistently [‡] until convergence of the whole set of governing equations in each time step. We couple our framework with an open-source package PETSc,[51] to employ its scalable nonlinear equation solvers as well as its linear Krylov subspace solvers.

4 | OCTREE-BASED MESH AND ADAPTIVE MESH REFINEMENT

The computational cost with fixed prerefined mesh is enormous because the position of the interface is constantly changing over time. As a result, in this work, we propose an octree mesh-based level set method that extends the level set method on an octree-based background mesh to achieve efficient adaptive mesh refinement following interface evolution, and therefore reduce the total computational effort.

4.1 | Octree mesh implementation

We employ the optimized parallel octree-based meshing library, Dendro, which provides the adaptive mesh refinement and all parallel data-structures. The process in Dendro used to build and maintain an adaptively refined octree mesh in parallel mainly includes following four parts:

- Refinement proceeding in a top-down fashion based on specific refining instructions. In this work, the interface with a finite thickness and near region are refined.
- 2:1 balancing which enforces that two neighboring octants differ in size by at most a factor of two. This allows a smooth transition in mesh density and makes subsequent operations simpler while retaining required adaptive properties.
- Partition based on a weighted space-filling-curve. Elements are equally partitioned by point-to-point communication to redistribute the elements across processes according to the number of elements in each process.
- Meshing that constructs the finite element computation data structures from the octree data structures. This also includes handling overlapping process boundary parts (shared nodes between neighboring processes).

The algorithms of above processes in Dendro are detailed in Reference 34. We also refer readers to References 33,52-55 for details on implementation of Dendro.

4.2 | Refinement according to interface location

To adapt the mesh refinement to resolve the large gradient inside the interface with a finite thickness, a uniform coarse mesh is first constructed. Proceeding in a top-down fashion, each cell in the mesh is refined if the interface covers,or partially covers it, which is determined using the level set field with the signed-distance property. If all eight corners of an octant are outside of the interface, that is, all corners have $\phi > \epsilon$ or $\phi < -\epsilon$, then we do not refine further. If all eight points are inside the interface, or at least one point is inside, that is, at least one corner have $-\epsilon < \phi < \epsilon$, then this

10970207, 2022, 22, Downloaded from https://onlinelibrary.wiley.com/doi/10.1002/nme.7077 by Harbin Insitute Of Technology, Wiley Online Library on [26/08/2023]. See the Terms and Conditions (https://onlinelibrary.wiley.com/terms-and-conditions) on Wiley Online Library for rules of use; OA articles are governed by the applicable Creative Commons License

octant is refined. This process is repeated until the desired level of refinement is achieved. Since considerable physics also takes place around gas-liquid interface, we extend the refinement to cover the near-interface region, that is, amplify the magnitude of ϵ during refinement. Note, The most refined (maximum refinement) region and most unrefined (minimum refinement) region will have a buffer region (intermediate refinement) between them, as seen in Figures 4, 6, 8A, due to the 2:1 balancing enforcement.

4.3 | Adaptive remeshing and intergrid transfers

Since we adaptively refine the mesh as the interface evolves, this indicates that we rebuild the octree hierarchy at each time step based on the current position of the interface using results of the level set field after redistancing. Note, rebuilding the octree also allows to coarsen a previously refined parent element, that is, merge children octants into a parent octant, once the interface moves away from the space. The reconstruction of octree structure is also followed by the procedures of 2:1 balancing, partition (to rebalance the load), and meshing as discussed in Section 4.1. Once the new mesh is adaptively constructed, we interpolate the data from the old mesh to the new mesh. Note when using the octree data-structure to regenerate new mesh, the intergrid transfer between old and new meshes only happens between parent and child (for refinement), or stays the same (for coarsening and unchanged elements), this can be first performed locally on the old mesh using standard linear interpolation, then followed by a repartitioning of the new mesh and interpolated data based on the new octree.

5 | RESULTS AND DISCUSSION

5.1 | Dam break without obstacles

We first simulate a three-dimensional (3D) dam break without obstacle in a unit cube to verify and validate the octree-based level set framework. A water column is restricted at the lower left wall with a height of $h_0 = 0.5$ m and a width of $w_0 = 0.25$ m. The densities of water and air are set to be 1000 and 1.2 kg/m^3, and the dynamic viscosities are set to be 1×10^{-3} and $1.8 \times 10^{-5}\text{kg/(m} \cdot \text{s)}$, respectively. Gravity acceleration is $g = 9.81\ \text{m/s}^2$. Time step is set to be 1×10^{-3} s. Note, there is no interfacial force considered in this case.

We first perform a mesh convergence study for the dam break problem. We choose three sets of meshes with a maximum refinement around the interface and a minimum refinement away from the interface. The min/max is set to be 3/5, 3/6, 4/7, resulting in initial number of total elements to be 7232, 30,976, and 116,992. An initial mesh (min/max refinement is 4/7) with local refinement around the interface is shown in Figure 1. Note, the total number of elements will vary

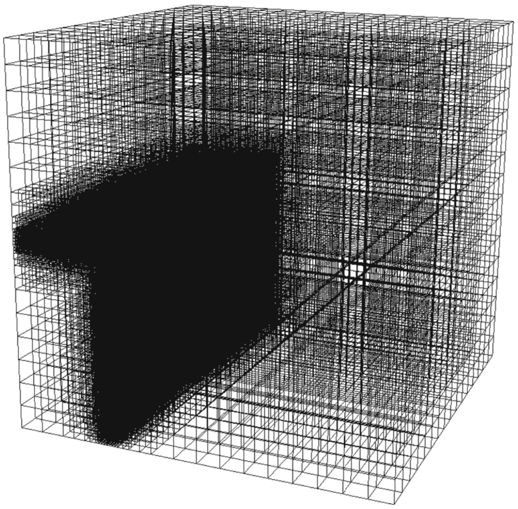

FIGURE 1 Initial mesh with local refinement around the interface for the dam break problem

10970207, 2022, 22, Downloaded from https://onlinelibrary.wiley.com/doi/10.1002/nme.7077 by Harbin Insitute Of Technology, Wiley Online Library on [26/08/2023]. See the Terms and Conditions (https://onlinelibrary.wiley.com/terms-and-conditions) on Wiley Online Library for rules of use; OA articles are governed by the applicable Creative Commons License

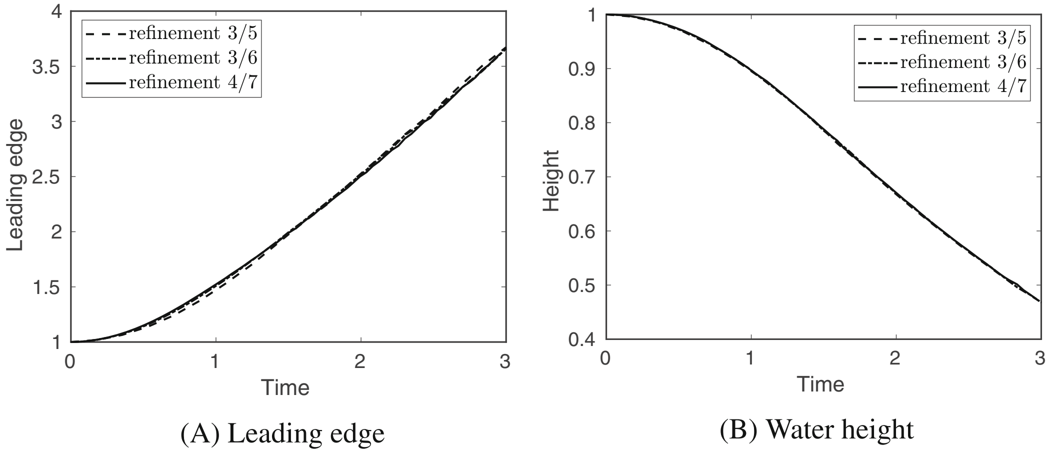

(A) Leading edge (B) Water height

FIGURE 2 Convergence results of leading edge and water height versus time for the dam break problem. Leading edge and height are normalized by w_0 and h_0, respectively, and time is normalized by $1/\sqrt{2g/w_0}$. (A) Leading edge and (B) water height

as the interface involves. The mesh convergence results of the water leading edge and height normalized by w_0 and h_0, respectively, as a function of time are shown in Figure 2.

We also compare the leading edge and water column height during evolution with some other experimental and numerical results[56-59] as shown in Figure 3. It can be seen that our results match the results from other references very well. We finally show the interface locations projected to the middle plane of the domain at four different time steps with adaptive mesh refinement around the interface in Figure 4.

5.2 | Single bubble rising

In this section, we simulate a single bubble rising in a quiescent liquid within a confined domain. Surface tension is considered as interfacial force in this case. We employ a cubic domain with dimension of 0.2 m × 0.2 m × 0.2 m. The spherical bubble is initially placed in the center of the domain with a diameter of $D = 0.01873$ m. The liquid and bubble densities are $\rho_f = 1000$ kg/m^3 and $\rho_g = 1$ kg/m^3, resulting in a density ratio of 1000. The liquid and bubble viscosities are $\mu_f = 0.527$ kg/(m · s) and $\mu_g = 0.00527$ kg/(m · s), resulting in a viscosity ratio of 100. The surface tension coefficient is $\sigma_s = 0.0141$ N/m. These physical parameters indicate two dimensionless parameters, Archimedes number, defined as $\frac{\rho_f g D^2}{\sigma_s}$, to be $Ar = 15.2$, and Bond number, defined as $\frac{\rho_f g^{1/2} D^{3/2}}{\mu_f}$, to be $Bo = 244$. Time step is chosen to be 2.5×10^{-4} s.

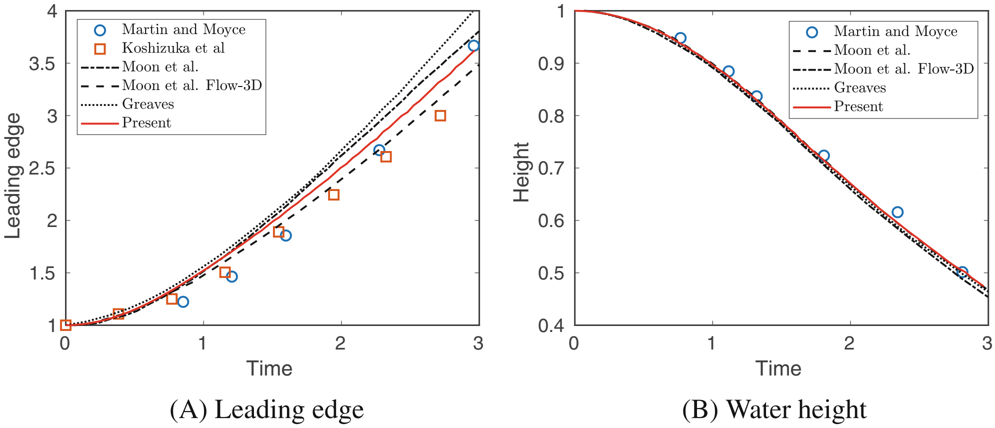

(A) Leading edge (B) Water height

FIGURE 3 Comparison of leading edge and water height versus time for the dam break problem. Leading edge and height are normalized by w_0 and h_0, respectively, and time is normalized by $1/\sqrt{2g/w_0}$. (A) Leading edge and (B) water height

10970207, 2022, 22, Downloaded from https://onlinelibrary.wiley.com/doi/10.1002/nme.7077 by Harbin Institute Of Technology, Wiley Online Library on [26/08/2023]. See the Terms and Conditions (https://onlinelibrary.wiley.com/terms-and-conditions) on Wiley Online Library for rules of use; OA articles are governed by the applicable Creative Commons License

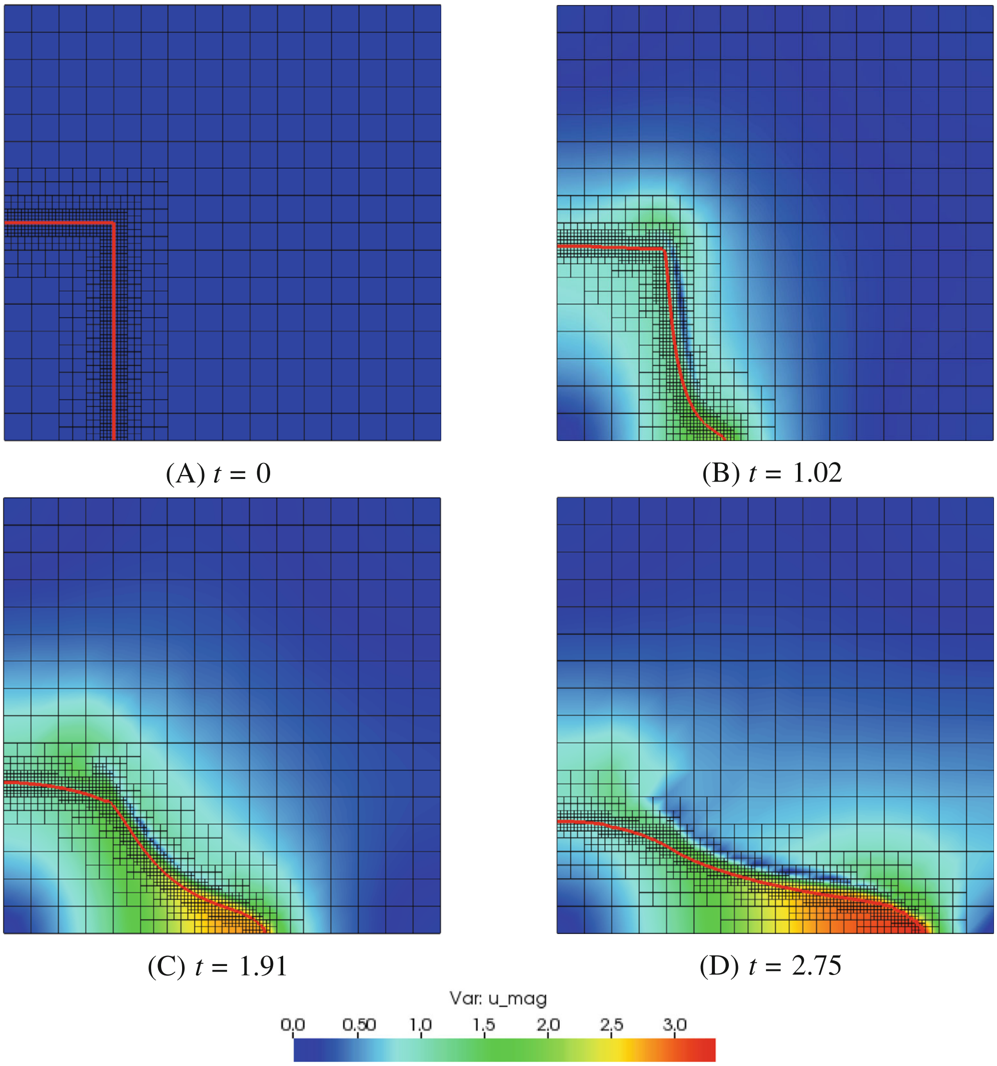
(A) $t = 0$

(B) $t = 1.02$

(C) $t = 1.91$

(D) $t = 2.75$

FIGURE 4 Interface on the center slice with adaptive mesh refinement at four different time steps for the dam break problem. Time is normalized by $1/\sqrt{2g/w_0}$. (A) $t = 0$; (B) $t = 1.02$; (C) $t = 1.91$; (D) $t = 2.75$

Two mesh densities with min/max refinements to be 5/8 and 5/9 are employed in this case, resulting in initial numbers of total elements to be 78,800 and 264,216. The dimensionless bubble rising velocity as a function of dimensionless time and terminal 3D bubble shape are plotted in Figure 5. It shows the two mesh densities produce similar results for the bubble motion and final shape, and similar bubble shapes can also be seen in References 60 (case A4), 13 (case D) and 61 (case A3). We compare the terminal Reynolds number, defined as $Re = \frac{\rho_f D u_\infty}{\mu_f}$, where u_∞ is the bubble terminal velocity, of these two mesh densities with other numerical and experimental results as shown in Table 1. It can be seen our results match the results from other references very well. In addition, the bubble shape projected to the middle plane of the domain at different time frames with adaptive mesh refinement around the interface is plotted for the mesh with min/max refinement of 5/9 in Figure 6.

For this example, we also show the scaling performance of the framework. We run the example with a min/max refinement level to be 7/10, and adjust the size of refinement region making the total number of degrees of freedom reach 43.2 million. We collect solve time for five time steps and take the average to obtain timing for one time step. The scaling test was performed on Stampede2, Texas Advanced Computer Center (TACC), using KNL compute nodes. We plot the performance for the example with different numbers of processes, in the style of a strong scaling for the solve time of one time step, as shown in Figure 7 (axes are plotted in log scale with base 2). Overall, the framework presents a good scalability with continued reductions in solve time up to 16,384 processes.

10970207, 2022, 22, Downloaded from https://onlinelibrary.wiley.com/doi/10.1002/nme.7077 by Harbin Institute Of Technology, Wiley Online Library on [26/08/2023]. See the Terms and Conditions (https://onlinelibrary.wiley.com/terms-and-conditions) on Wiley Online Library for rules of use; OA articles are governed by the applicable Creative Commons License

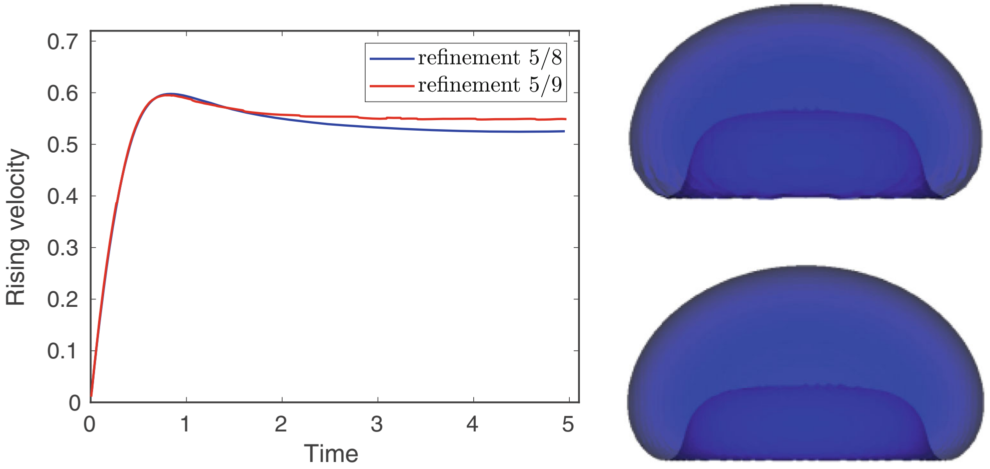

(A) Bubble motion (B) Bubble shape

FIGURE 5 (A) Dimensionless rising velocity v.s. time for the bubble rising problem. Velocity is normalized by $\sqrt{gD}$, and time is normalized by $\sqrt{D/g}$. (B) Terminal three-dimensional bubble shape for min/max mesh refinement: (upper) 5/8, and (lower) 5/9. (A) Bubble motion; (B) Bubble shape

TABLE 1 Comparison of terminal Reynolds number for the bubble rising problem

This work (min/max refinement)	References
7.99 (5/8), 8.35 (5/9)	8.40,[60] 7.60[61]

5.3 | Thermocapillary droplet migration

5.3.1 | Without gravity

In this section, we simulate a thermocapillary droplet migration in an ambient liquid with a linear initial temperature profile. We employ a cubic domain with dimension of 0.03 m × 0.03 m × 0.03 m, which is large enough to eliminate boundary effect according to Reference 62. The droplet is initially placed in the center of the domain with a radius of $R = 1.44 \times 10^{-3}$ m. The liquid density, viscosity, specific heat, and thermal conductivity are $\rho_f = 500\ \text{kg/m}^3$, $\mu_f = 0.024\ \text{kg/(m} \cdot \text{s)}$, $cp_f = 10^{-4}$ and $\kappa_f = 2.4 \times 10^{-6}\ \text{W/(m} \cdot \text{K)}$. The ratios of the material properties between the droplet and ambient liquid is chosen to be 0.5. The surface tension coefficient is $\sigma_s = 0.01\ \text{N/m}$, and Marangoni coefficient is $\frac{d\sigma_s}{dT} = 2 \times 10^{-3}\ \text{N/(m} \cdot \text{K)}$. These physical parameters indicate three dimensionless parameters, the Reynolds number, defined as $Re = \frac{\rho_f R u_r}{\mu_f}$, to be 0.72, where u_r is the reference velocity, defined as $u_r = \frac{d\sigma_s}{dT}|\nabla T|R/\mu_f$, the Marangoni number, defined as $Ma = \frac{\rho_f cp_f R u_r}{\kappa_f}$, to be 0.72, and the Capillary number, defined as $Ca = \frac{\mu_f u_r}{\sigma_s}$, to be 0.0576. Initial temperature is specified as a high temperature of 276 K at the top wall, a low temperature of 270 K at the bottom wall, and a linear temperature distribution along the vertical direction in the interior of the domain, resulting in a constant temperature gradient of 200 K/m along the vertical direction. No slip boundary condition and fixed temperature at horizontal walls are specified. Note, gravity is not considered while surface tension and Marangoni effect as interfacial force are considered in this case. Since gravity is ignored, surface tension in the normal direction of the droplet surface will keep the droplet shape unchanged. The Marangoni stress in the tangential direction of the droplet surface will drive the droplet to move along the vertical direction (i.e., the direction of temperature gradient). Time step is chosen to be 10^{-3} s.

We employ a mesh with min/max refinement to be 5/8, and show the local refinement around the interface projected in the middle plane of the domain as seen in Figure 8A. Velocity vectors with temperature contour lines are plotted in Figure 8C. Recirculation vortex can be observed in both sides inside the droplet, and similar flow pattern is also exhibited in other references.[48,62] We finally plot the dimensionless migration velocity as a function of dimensionless time in Figure 8B, and compare with other numerical and analytical results.[48,62,63] A good agreement is presented between our

10970207, 2022, 22, Downloaded from https://onlinelibrary.wiley.com/doi/10.1002/nme.7077 by Harbin Institute Of Technology, Wiley Online Library on [26/08/2023]. See the Terms and Conditions (https://onlinelibrary.wiley.com/terms-and-conditions) on Wiley Online Library for rules of use; OA articles are governed by the applicable Creative Commons License

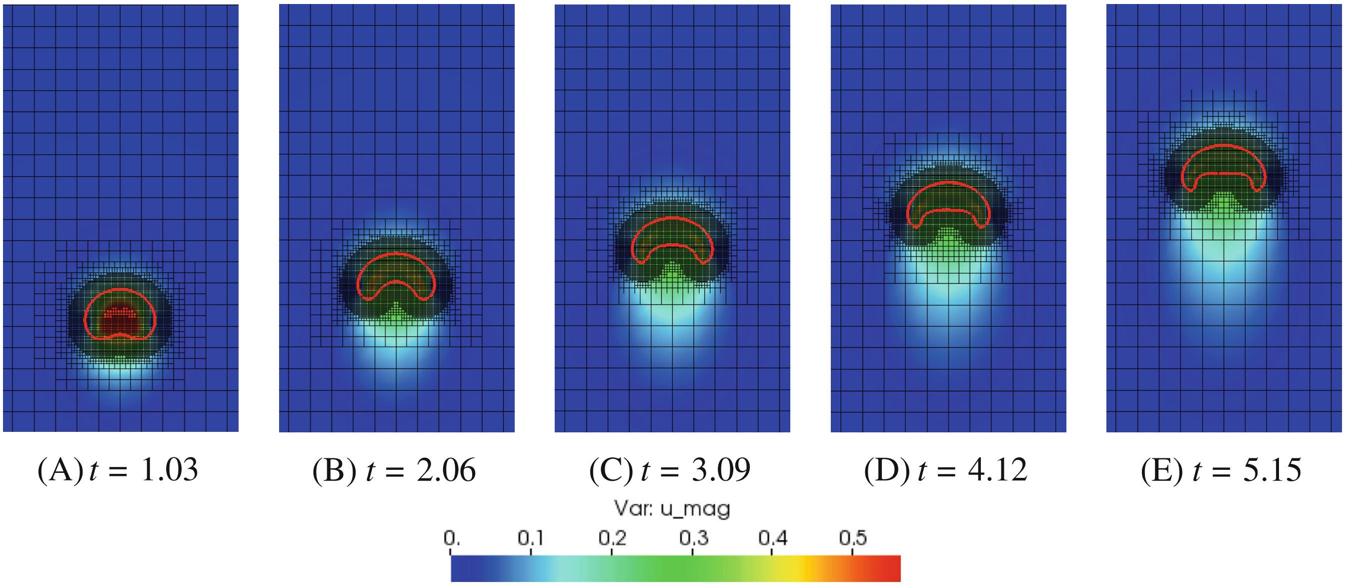

FIGURE 6 Bubble shape on the center slice with adaptive mesh refinement at five different time steps for the bubble rising problem. Time is normalized by $\sqrt{D/g}$. (A) $t = 1.03$; (B) $t = 2.06$; (C) $t = 3.09$; (D) $t = 4.12$; (E) $t = 5.15$

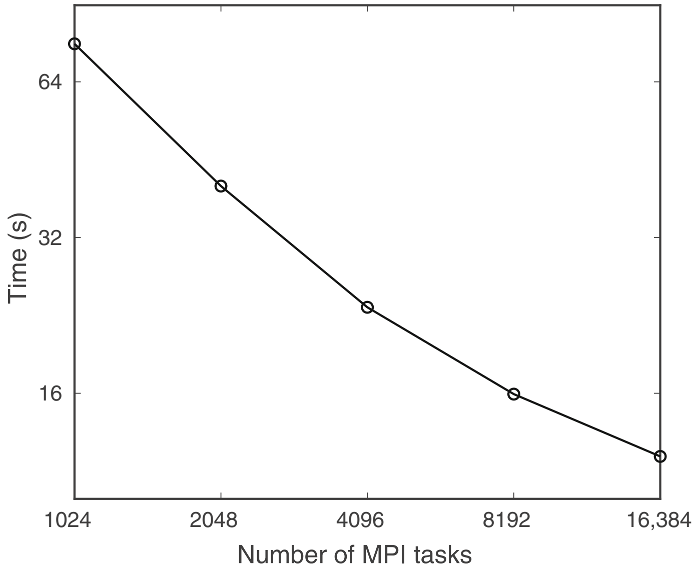

FIGURE 7 Strong scaling of averaged one time step solve time for the bubble rising problem with 43.2 million degrees of freedom with number of processes up to 16,384 on Stampede2.

results and results from other numerical approaches, while a discrepancy between Young et al.'s[63] analytical result and all other numerical results is notable, for which we speculate is due to the assumptions of infinite domain and Stokes flow in the analytical result.

5.3.2 | With gravity

In this section, the gravity for the problem of thermocapillary droplet migration is considered. Similar dimensionless scaling is employed as the previous section, and some resulting dimensionless parameters are $Re = 8$, $Ma = 56$, and

10970207, 2022, 22, Downloaded from https://onlinelibrary.wiley.com/doi/10.1002/nme.7077 by Harbin Institute Of Technology, Wiley Online Library on [26/08/2023]. See the Terms and Conditions (https://onlinelibrary.wiley.com/terms-and-conditions) on Wiley Online Library for rules of use; OA articles are governed by the applicable Creative Commons License

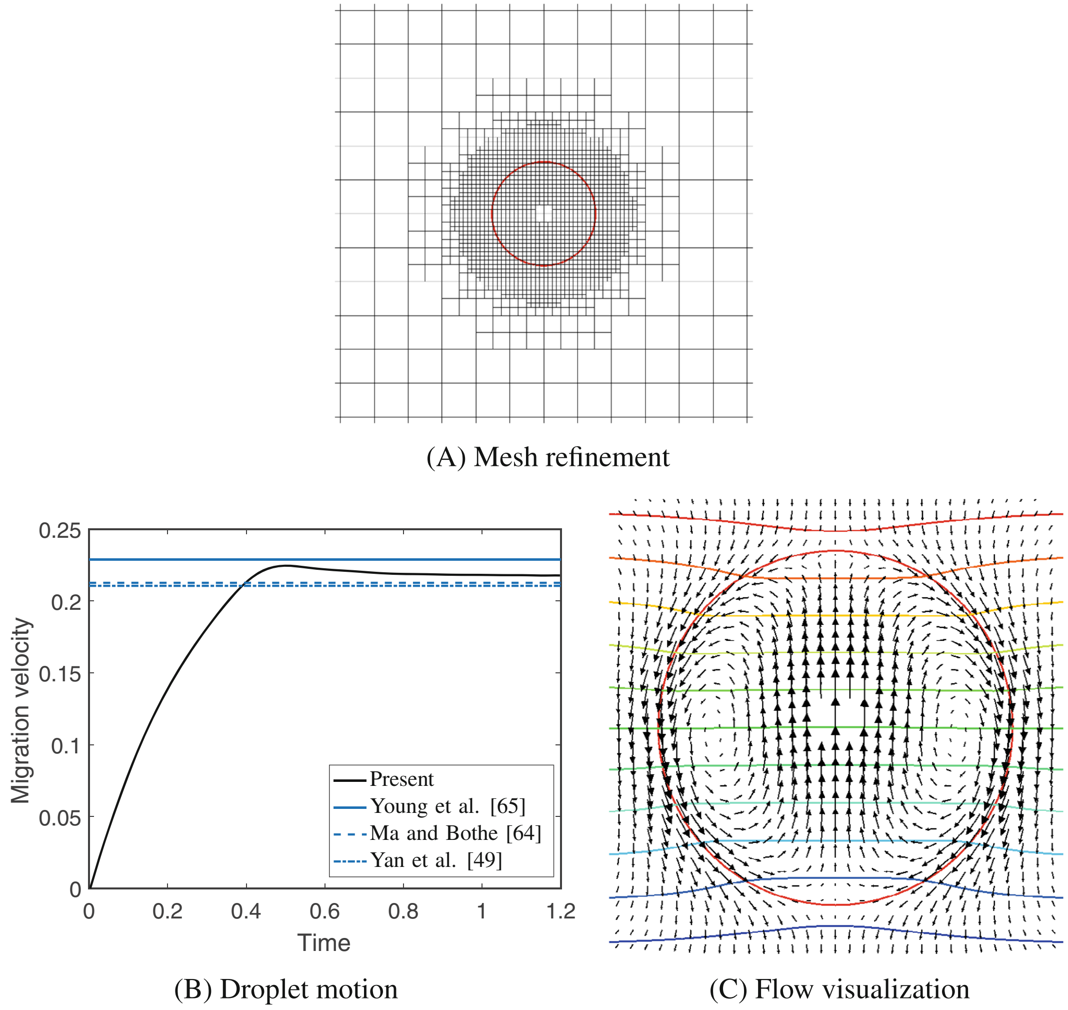

(A) Mesh refinement

(B) Droplet motion

(C) Flow visualization

FIGURE 8 (A) Local mesh refinement around the interface for the problem of thermocapillary droplet migration without gravity. (B) Dimensionless migration velocity versus time and comparison with other approaches. Velocity is normalized by u_r, and time is normalized by R/u_r. (C) Velocity vectors with temperature contour lines. (A) Mesh refinement; (B) droplet motion; (C) flow visualization

$Ca = 0.032$. Besides, Froude number and Prandtl number are introduced, and defined as $Fr = \frac{U_r^2}{gR}$ to be 6.4, and $Pr = \frac{\nu_f}{\alpha_f}$ to be 7, respectively, where ν_f is kinetic viscosity and $\alpha_f = \frac{\kappa_f}{\rho_f c p_f}$ is the thermal diffusivity. Another two temperature-related parameters are also defined, that is, dimensionless temperature gradient $\beta = \frac{\nabla T}{R} T_{\text{ref}}$ to be 0.1, and dimensionless Marangoni coefficient $M = \frac{d\sigma_s}{dT} T_{\text{ref}}/\sigma_s$ to be 0.32, where T_{ref} is the reference temperature. A positive M indicates that the Marangoni stress acts on the droplet surface along with the same direction of the buoyancy. Note, above definitions produce $Ca = M\beta$ and $Ma = RePr$. In addition, the relative density, viscosity, and diffusivity of the two materials are $\frac{\rho_g}{\rho_f} = 10^{-3}$, $\frac{\mu_g}{\mu_f} = 10^{-2}$, and $\frac{\alpha_g}{\alpha_f} = 4 \times 10^{-2}$. The rest of computational setup is similar as the previous section.

Figure 9 shows the isotherms and the shapes of the droplet in the vertical median plane at different time steps, and Figure 10A exhibits the variation of vertical coordinate of the droplet center along with time. In contrast to the previous case without buoyancy, where the droplet shape is kept spherical due to surface tension, in this case the droplet eventually deforms to an oblate shape. Similar behavior of the droplet under gravity can also be found in Reference 64. Figure 10B quantitatively demonstrates the shape of droplet at dimensionless time $t = 10$, and plots the distance of the points on the droplet surface in the vertical median plane to the droplet center. The radian in Figure 10B starts from the point with minimum horizontal coordinate and moves clockwise. Since buoyancy is considered, the resulting effect of inertial force dominates the flow as opposed to the previous case, and overshadows the surface tension, which alters the droplet shape.

10970207, 2022, 22, Downloaded from https://onlinelibrary.wiley.com/doi/10.1002/nme.7077 by Harbin Institute Of Technology, Wiley Online Library on [26/08/2023]. See the Terms and Conditions (https://onlinelibrary.wiley.com/terms-and-conditions) on Wiley Online Library for rules of use; OA articles are governed by the applicable Creative Commons License

10970207, 2022, 22, Downloaded from https://onlinelibrary.wiley.com/doi/10.1002/nme.7077 by Harbin Insitute Of Technology, Wiley Online Library on [26/08/2023]. See the Terms and Conditions (https://onlinelibrary.wiley.com/terms-and-conditions) on Wiley Online Library for rules of use; OA articles are governed by the applicable Creative Commons License

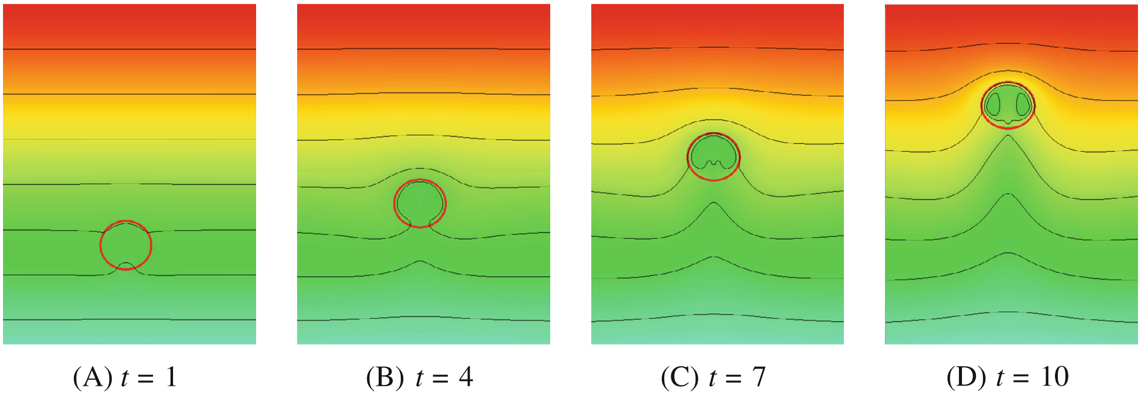

FIGURE 9 Isotherms and shapes of the droplet in the vertical median plane at different time steps for the problem of thermocapillary droplet migration with gravity. (A) t = 1 (B) t = 4 (C) t = 7 (D) t = 10

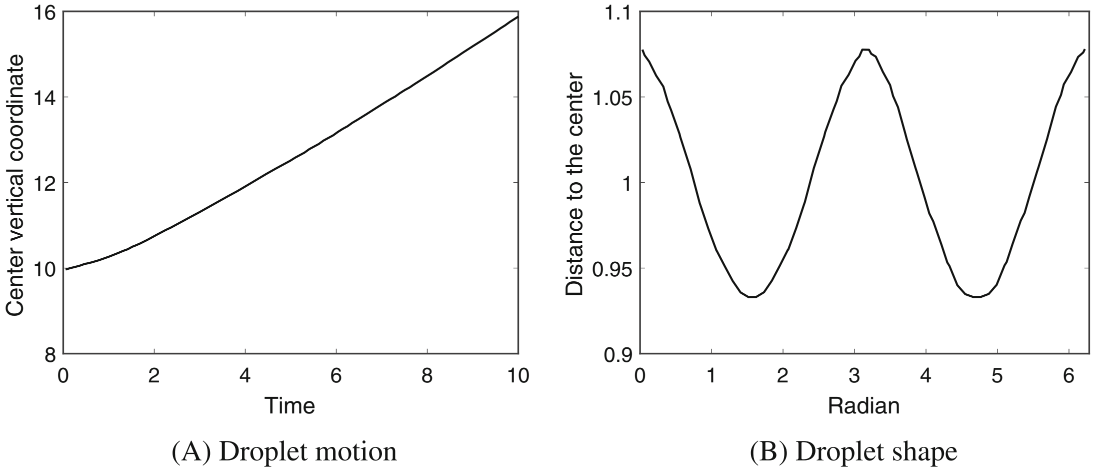

FIGURE 10 (A) Variation of vertical coordinate of the droplet center v.s. time for the problem of thermocapillary droplet migration with gravity. (B) Distance of the points on the droplet surface in the vertical median plane to the droplet center.

6 | CONCLUSIONS AND FUTURE WORK

We develop a parallel finite element computational framework based on level set method on adaptive octree meshes for thermal free surface flows. The sharp gas–liquid interface is regularized in the spacial discretization, and redistancing of the level set field and restoration of mass conservation after each time step are performed in the framework. Interfacial forces are considered via a CSF model. The octree mesh is adaptively refined according to the interface location, and the load is rebalanced across processes followed by interpolation between meshes. The discretized governing equations are stabilized using a residual-based VMS method. The adaptive octree-based level set framework is verified and validated using multiple canonical problems including dam break without obstacle, single bubble rising in ambient liquid and thermocapillary droplet migration with and without gravity. We also present the parallel scaling performance for the bubble rising problem to illustrate the good scalability of the method. The results in this paper have demonstrated the robustness and accuracy of our framework in simulating free-surface flows under various physics scenarios. We anticipate to further consider phase change into this framework and deploy it to additive manufacturing in the future.

ACKNOWLEDGMENTS

The authors greatly appreciate computing resources provided by the University of Utah Center for High-Performance Computing (CHPC), and XSEDE grant number TG-MSS200020 for computing time on Stampede2, Texas Advanced Computer Center (TACC).

ENDNOTES

[*] Equation (29) can be essentially interpreted as a pseudo time-dependent Eikonal equation.

[†] The first line of Equation (31) can be rewritten as $\int_\Omega \eta_{rd}^h \left(\frac{\partial \phi_{rd}^h}{\partial t_{rd}} + S_{rd}\left(\phi_{rd}^h\right) \frac{\nabla \phi_{rd}^h}{|\nabla \phi_{rd}^h|} \cdot \nabla \phi_{rd}^h - S_{rd}\left(\phi_{rd}^h\right) \right) \, d\Omega$.

[‡] When solving variables for one system, treat the variables from the other two systems constant with their most recently updated values.

ORCID

Songzhe Xu https://orcid.org/0000-0003-4108-3503

REFERENCES

1. Prosperetti A, Tryggvason G. *Computational Methods for Multiphase Flow*. Cambridge University Press; 2009.
2. Tezduyar TE. Finite element methods for flow problems with moving boundaries and interfaces. *Arch Comput Methods Eng*. 2001;8:83-130. doi:10.1007/BF02897870
3. Hughes TJR, Liu WK, Zimmermann TK. Lagrangian–Eulerian finite element formulation for incompressible viscous flows. *Comput Methods Appl Mech Eng*. 1981;29:329-349.
4. Best JP. The formation of toroidal bubbles upon the collapse of transient cavities. *J Fluid Mech*. 1993;251:79-107.
5. Unverdi SO, Tryggvason G. A front-tracking method for viscous, incompressible, multi-fluid flows. *J Comput Phys*. 1992;100(1):25-37.
6. Braess H, Wriggers P. Arbitrary Lagrangian Eulerian finite element analysis of free surface flow. *Comput Methods Appl Mech Eng*. 2000;190(1-2):95-109.
7. Gan Z, Yu G, He X, Li S. Numerical simulation of thermal behavior and multicomponent mass transfer in direct laser deposition of co-base alloy on steel. *Int J Heat Mass Transf*. 2017;104:28-38.
8. Shirani E, Ashgriz N, Mostaghimi J. Interface pressure calculation based on conservation of momentum for front capturing methods. *J Comput Phys*. 2005;203(1):154-175.
9. Jacqmin D. Calculation of two-phase Navier–Stokes flows using phase-field modeling. *J Comput Phys*. 1999;155(1):96-127.
10. Liu J. *Thermodynamically Consistent Modeling and Simulation of Multiphase Flows*. PhD thesis.
11. Hirt CW, Nichols BD. Volume of fluid (VOF) method for the dynamics of free boundaries. *J Comput Phys*. 1981;39:201-225.
12. Yue P, Feng JJ, Liu C, Shen J. A diffuse-interface method for simulating two-phase flows of complex fluids. *J Fluid Mech*. 2004;515:293-317.
13. Amaya-Bower L, Lee T. Single bubble rising dynamics for moderate Reynolds number using lattice Boltzmann method. *Comput Fluids*. 2010;39(7):1191-1207.
14. Sussman M, Smereka P, Osher S. A level set approach for computing solutions to incompressible two-phase flow. *J Comput Phys*. 1994;114(1):146-159.
15. Osher S, Sethian JA. Fronts propagating with curvature-dependent speed: algorithms based on hamilton-jacobi formulations. *J Comput Phys*. 1988;79(1):12-49.
16. Calderer R, Zhu L, Gibson R, Masud A. Residual-based turbulence models and arbitrary Lagrangian–Eulerian framework for free surface flows. *Math Models Methods Appl Sci*. 2015;25(12):2287-2317.
17. Zhu L, Goraya S, Masud A. A stabilized interface capturing method for large amplitude breaking waves. *J Eng Mech*. 2019;145(11):04019088.
18. Gimenez JM, Nigro NM, Idelsohn SR, Oñate E. Surface tension problems solved with the particle finite element method using large time-steps. *Comput Fluids*. 2016;141:90-104.
19. Nagrath S, Jansen KE, Lahey RT. Computation of incompressible bubble dynamics with a stabilized finite element level set method. *Comput Methods Appl Mech Eng*. 2005;194(42):4565-4587.
20. Tripathi MK, Sahu KC, Govindarajan R. Dynamics of an initially spherical bubble rising in quiescent liquid. *Nat Commun*. 2015;6(1):1-9.
21. Van Sint Annaland M, Deen NG, Kuipers JAM. Numerical simulation of gas bubbles behaviour using a three-dimensional volume of fluid method. *Chem Eng Sci*. 2005;60(11):2999-3011.
22. Bielak J, Ghattas O, Kim EJ. Parallel octree-based finite element method for large-scale earthquake ground motion simulation. *Comput Model Eng Sci*. 2005;10(2):99.
23. Becker R, Braack M. Multigrid techniques for finite elements on locally refined meshes. *Numer Linear Algebra Appl*. 2000;7(6):363-379.
24. Legrain G, Allais R, Cartraud P. On the use of the extended finite element method with quadtree/octree meshes. *Int J Numer Methods Eng*. 2011;86(6):717-743.
25. Thieulot C, Fullsack P, Braun J. Adaptive octree-based finite element analysis of two-and three-dimensional indentation problems. *J Geophys Res*. 2008;113:B12207.
26. Patra AK, Laszloffy A, Long J. Data structures and load balancing for parallel adaptive hp finite-element methods. *Comput Math Appl*. 2003;46(1):105-123.
27. Flaherty JE, Loy RM, Özturan C, et al. Parallel structures and dynamic load balancing for adaptive finite element computation. *Appl Numer Math*. 1998;26(1-2):241-263.
28. Fernando M, Neilsen D, Lim H, Hirschmann E, Sundar H. Massively parallel simulations of binary black hole intermediate-mass-ratio inspirals. *SIAM J Sci Comput*. 2019;41(2):C97-C138.

10970207, 2022, 22, Downloaded from https://onlinelibrary.wiley.com/doi/10.1002/nme.7077 by Harbin Institute Of Technology, Wiley Online Library on [26/08/2023]. See the Terms and Conditions (https://onlinelibrary.wiley.com/terms-and-conditions) on Wiley Online Library for rules of use; OA articles are governed by the applicable Creative Commons License

29. Saurabh K, Gao B, Fernando M, et al. Industrial scale large eddy simulations with adaptive octree meshes using immersogeometric analysis. *Comput Math Appl*. 2021;97:28-44.
30. Xu S, Gao B, Lofquist A, et al. An octree-based immersogeometric approach for modeling inertial migration of particles in channels. *Comput Fluids*. 2021;214:104764.
31. Khanwale MA, Lofquist AD, Sundar H, Rossmanith JA, Ganapathysubramanian B. Simulating two-phase flows with thermodynamically consistent energy stable Cahn-Hilliard Navier-stokes equations on parallel adaptive octree based meshes. *J Comput Phys*. 2020;419:109674.
32. Ishii M, Fernando M, Saurabh K, Khara B, Ganapathysubramanian B, Sundar H. Solving pdes in space-time: 4D tree-based adaptivity, mesh -free and matrix- free approaches. Proceedings of the International Conference for High Performance Computing, Networking, Storage and Analysis, SC '19; 2019:61:1-61:61; ACM.
33. Sundar H, Sampath RS, Adavani SS, Davatzikos C, Biros G. Low-constant parallel algorithms for finite element simulations using linear octrees. Proceedings of the International Conference for High Performance Computing, Networking, Storage, and Analysis SC'07; 2007; ACM/IEEE.
34. Sundar H, Sampath RS, Biros G. Bottom-up construction and 2: 1 balance refinement of linear octrees in parallel. *SIAM J Sci Comput*. 2008;30(5):2675-2708.
35. Tu T, O'Hallaron DR, Ghattas O. Scalable parallel octree meshing for terascale applications. Proceedings of the 2005 ACM/IEEE Conference on Supercomputing; 2005:4; IEEE Computer Society.
36. Warren MS, Salmon JK. A parallel hashed Oct-tree N-body algorithm. Proceedings of the Supercomputing '93; 1993:12-21.
37. Ying L, Biros G, Zorin D, Langston H. A new parallel kernel-independent fast multipole method. Proceedings of the 2003 ACM/IEEE Conference on Supercomputing SC'03; 2003:14-14; IEEE.
38. Bazilevs Y, Calo VM, Cottrell JA, Hughes TJR, Reali A, Scovazzi G. Variational multiscale residual-based turbulence modeling for large eddy simulation of incompressible flows. *Comput Methods Appl Mech Eng*. 2007;197:173-201.
39. Xu S, Liu N, Yan J. Residual-based variational multi-scale modeling for particle-laden gravity currents over flat and triangular wavy terrains. *Comput Fluids*. 2019;188:114-124.
40. Xu S, Gao B, Hsu M-C, Ganapathysubramanian B. A residual-based variational multiscale method with weak imposition of boundary conditions for buoyancy-driven flows. *Comput Methods Appl Mech Eng*. 2019;352:345-368.
41. Yan J, Korobenko A, Tejada-Martínez AE, Golshan R, Bazilevs Y. A new variational multiscale formulation for stratified incompressible turbulent flows. *Comput Fluids*. 2016;158:150-156.
42. Van Opstal TM, Yan J, Coley C, Evans JA, Kvamsdal T, Bazilevs Y. Isogeometric divergence-conforming variational multiscale formulation of incompressible turbulent flows. *Comput Methods Appl Mech Eng*. 2016;316:859-879.
43. Xu F, Xu S, Passe U, Ganapathysubramanian B. Computational study of natural ventilation in a sustainable building with complex geometry. *Sustain Energy Technol Assess*. 2021;45:101153.
44. Yan J, Korobenko A, Deng X, Bazilevs Y. Computational free-surface fluid–Structure interaction with application to floating offshore wind turbines. *Comput Fluids*. 2016;141:155-174.
45. Yan J, Deng X, Korobenko A, Bazilevs Y. Free-surface flow modeling and simulation of horizontal-axis tidal-stream turbines. *Comput Fluids*. 2016;158:157-166.
46. Yan J, Lin S, Bazilevs Y, Wagner GJ. Isogeometric analysis of multi-phase flows with surface tension and with application to dynamics of rising bubbles. *Comput Fluids*. 2019;179:777-789.
47. Zhu Q, Xu F, Xu S, Hsu M, Yan J. An immersogeometric formulation for free-surface flows with application to marine engineering problems. *Comput Methods Appl Mech Eng*. 2020;361:112748.
48. Yan J, Yan W, Lin S, Wagner GJ. A fully coupled finite element formulation for liquid–Solid–Gas thermo-fluid flow with melting and solidification. *Comput Methods Appl Mech Eng*. 2018;336:444-470.
49. Zhu Q, Yan J. A mixed interface-capturing/interface-tracking formulation for thermal multi-phase flows with emphasis on metal additive manufacturing processes. *Comput Methods Appl Mech Eng*. 2021;383:113910.
50. Hamilton WR. Theory of systems of rays. *Trans Royal Irish Acad*. 1828;15:69-174.
51. Balay S, Abhyankar S, Adams MF, et al. PETSc users manual. Technical Report ANL-95/11 - Revision 3.10, Argonne National Laboratory, 2018. http://www.mcs.anl.gov/petsc
52. Bern M, Eppstein D, Teng S-H. Parallel construction of quadtrees and quality triangulations. *Int J Comput Geom Appl*. 1999;9(6):517-532.
53. Burstedde C, Wilcox LC, Ghattas O. p4est: scalable algorithms for parallel adaptive mesh refinement on forests of octrees. *SIAM J Sci Comput*. 2011;33(3):1103-1133.
54. Sundar H, Biros G, Burstedde C, Rudi J, Ghattas O, Stadler G. Parallel geometric-algebraic multigrid on unstructured forests of octrees. Proceedings of the International Conference on High Performance Computing, Networking, Storage and Analysis, SC '12; 2012:43:1-43:11; Los Alamitos, CA, IEEE Computer Society Press. http://dl.acm.org/citation.cfm?id=2388996.2389055.
55. Fernando M, Duplyakin D, Sundar H. Machine and application aware partitioning for adaptive mesh refinement applications. Proceedings of the 26th International Symposium on High-Performance Parallel and Distributed Computing; 2017:231-242; ACM.
56. Moon WC, Puay HT, Lau TL. Numerical simulation of free surface flow using a multiphase model with higher order scheme. Proceedings of the AIP Conference Proceedings; 2020:020078; AIP Publishing LLC.
57. Greaves DM. Simulation of viscous water column collapse using adapting hierarchical grids. *Int J Numer Methods Fluids*. 2006;50(6):693-711.
58. Koshizuka S, Oka Y. Moving-particle semi-implicit method for fragmentation of incompressible fluid. *Nucl Sci Eng*. 1996;123(3):421-434.

10970207, 2022, 22, Downloaded from https://onlinelibrary.wiley.com/doi/10.1002/nme.7077 by Harbin Institute Of Technology, Wiley Online Library on [26/08/2023]. See the Terms and Conditions (https://onlinelibrary.wiley.com/terms-and-conditions) on Wiley Online Library for rules of use; OA articles are governed by the applicable Creative Commons License

59. Martin JC, Moyce W, Penney W, Price AT, Thornhill CK. Part IV. an experimental study of the collapse of liquid columns on a rigid horizontal plane. *Philos Trans Royal Soc Lond Ser A Math Phys Sci*. 1952;244:312-324.
60. Hua J, Lou J. Numerical simulation of bubble rising in viscous liquid. *J Comput Phys*. 2007;222(2):769-795.
61. Hua J, Stene JF, Lin P. Numerical simulation of 3d bubbles rising in viscous liquids using a front tracking method. *J Comput Phys*. 2008;227(6):3358-3382.
62. Ma C, Bothe D. Direct numerical simulation of thermocapillary flow based on the volume of fluid method. *Int J Multiphase Flow*. 2011;37(9):1045-1058.
63. Young NO, Goldstein JS, Block MJ. The motion of bubbles in a vertical temperature gradient. *J Fluid Mech*. 1959;6(3):350-356.
64. Tripathi MK, Sahu KC. Motion of an air bubble under the action of thermocapillary and buoyancy forces. *Comput Fluids*. 2018;177:58-68.

How to cite this article: Xu S, Zhu Q, Fernando M, Sundar H. A finite element level set method based on adaptive octree meshes for thermal free-surface flows. *Int J Numer Methods Eng*. 2022;123(22):5500-5516. doi: 10.1002/nme.7077

10970207, 2022, 22, Downloaded from https://onlinelibrary.wiley.com/doi/10.1002/nme.7077 by Harbin Insitute Of Technology, Wiley Online Library on [26/08/2023]. See the Terms and Conditions (https://onlinelibrary.wiley.com/terms-and-conditions) on Wiley Online Library for rules of use; OA articles are governed by the applicable Creative Commons License